frontiers | Frontiers in Materials

TYPE Original Research
PUBLISHED 14 August 2024
DOI 10.3389/fmats.2024.1461198

OPEN ACCESS

EDITED BY
Di Wang,
University of Ottawa, Canada

REVIEWED BY
Teng Wang,
University of Pisa, Italy
Fucheng Guo,
Lanzhou Jiaotong University, China

*CORRESPONDENCE
Lu Jin,
skd991767@sdust.edu.cn

RECEIVED 08 July 2024
ACCEPTED 26 July 2024
PUBLISHED 14 August 2024

CITATION
Ding Z, Cheng Y, Jin L, Wang W and Yan S (2024) Study on the strength characteristics and micro-mechanism of modified solidified red mud.
Front. Mater. 11:1461198.
doi: 10.3389/fmats.2024.1461198

Study on the strength characteristics and micro-mechanism of modified solidified red mud

Ziyi Ding, Yu Cheng, Lu Jin*, Wentong Wang and Shiying Yan

College of Transportation, Shandong University of Science and Technology, Qingdao, China

The residue generated during the production process of alumina, known as red mud, is a type of solid waste. The engineering properties of red mud can be significantly enhanced through the modification and solidification using inorganic materials. This study primarily utilized red mud as the raw material, supplemented with fly ash, lime, and clay, to conduct a solidification experiment of red mud. Orthogonal tests with three factors of two ash ratio (ratio of lime to fly ash), two ash content (total lime and fly ash), and red mud types were designed to study the changes of different ratios and maintenance conditions, etc., on the engineering properties of red mud. In addition, the micro-mechanisms of modified red mud were investigated by means of XRF, XRD, SEM and EDX. The results show that for optimum moisture content, red mud types are the most important influencing factor and for maximum dry density, two ash content is the most important influencing factor. For strength characteristics, the optimum two ash ratio was 1.5:1, the optimum two ash content was 50%, and the optimum red mud types were 70% CRM (red mud made of Chalco Shandong Co., Ltd) mixed with 30% clay. The addition of lime, fly ash, and clay improves the temperature shrinkage coefficient of the red mud. Through the analysis of microscopic composition and structure, it can be seen that goethite (α-FeO(OH)) and magnetite (γ-Fe_2O_3) in the red mud reacted with the modified materials to generate crystalline aluminosilicate and amorphous hydrated silicate gel, and these products together with the original calcium carbonate ($CaCO_3$), tricalcium aluminate (Ca3Al2O6) and garnet ($Ca_3TiFeSi_3O_{12}$) in the red mud which have certain strengths enhance the structural strength of the modified red mud. The optimum ratio obtained from the combined test results was lime: fly ash: CRM = 30:20:50. Therefore, using lime, fly ash and clay as modified materials can greatly enhance the engineering properties of red mud and realise the resourceful use of red mud.

KEYWORDS

red mud, modification treatment, orthogonal test, engineering characteristics, micro-mechanism

1 Introduction

Red mud is a solid waste generated during the extraction of alumina in the aluminum industry, with different properties according to different processes, but mostly reddish-brown powder with a fine particle size. Approximately 0.8–2 tons of red mud are discharged for every ton of alumina produced. As of 2022, China's annual production of alumina reaches

79.76 million tons, accounting for 57.4% of the global admixture. Nevertheless, despite the fact that the total volume of red mud stockpiled in China has exceeded one billion tons and that the annual addition of red mud exceeds one hundred million tons, its comprehensive utilization rate of the total red mud is less than 10% (Da et al., 2022). It is evident that the management and comprehensive utilization of red mud is lagging behind the growth rate of the alumina industry. Due to the unique process of alumina production, the red mud produced is distinguished by high alkalinity, a complex composition, and the presence of radioactive heavy metal ions, which can result in significant environmental contamination if stored in large quantities or applied directly (Khairul et al., 2019). The accumulation of red mud consumes land, pollutes nearby soil and groundwater, and disrupts daily life and industrial operations (Vigneshwaran et al., 2020). In order to achieve carbon neutrality and peak carbon, the construction industry has carried out a series of explorations, using cutting-edge technologies for intelligent buildings is one research direction (Shan et al., 2024) and recycling of solid waste is another (Wei et al., 2024). The research in this paper focuses on another direction: the modified solidification treatment of solid waste as a building material.

The principal chemical composition of red mud comprises calcium oxide (CaO), silicon dioxide (SiO_2), aluminum oxide (Al_2O_3), and iron oxide (Fe_2O_3), in addition to a number of amorphous silica-aluminate compounds (Luo et al., 2019). The external pressure and temperature exerted upon red mud result in a process of hardening, which gives rise to the formation of a crystalline network structure. This provides strength and produces strong semi-rigid plates, thereby creating a robust spatial network (Hu et al., 2021). Recent studies have demonstrated that low-cost industrial solid wastes, including fly ash, blast furnace slag, carbide slag, and phosphogypsum, can be employed to stabilize and solidify red mud (Qiang et al., 2022; Essaid et al., 2023). The incorporation of modified curing materials into red mud and the application of mechanical compaction results in a series of physicochemical reactions between red mud particles, leading to the formation of various hydrates, such as calcium silicate hydrates, around the particles. These hydrates adsorb and solidify soluble alkali ions such as Na^+ and K^+ (Xi et al., 2022). Furthermore, red mud also has some degree of hydraulic activity and can be used as an active supplementary material in cement. The utilization of red mud as a concrete admixture enables the production of concrete materials with the requisite strength and durability for engineering applications (Department of Architectural Engineering et al., 2020). The utilization of asphalt has a long history, and some scholars have studied the addition of industrial solid waste to improve the properties of asphalt (Falchetto et al., 2018; Walther et al., 2019a; Walther et al., 2019b; Lily et al., 2022; Wangjie et al., 2024), and studied the effect of different maintenance conditions on asphalt (Sun et al., 2020a; Sun et al., 2020b), which is instructive for the utilization of red mud. Venkatesh et al. found that the compressive strength of concrete with 10% cement replaced by red mud was increased by 12.78% as compared to that of cemented concrete. Hou et al. (Dongshuai et al., 2021) demonstrated the use of red mud in the production of ultra-high-performance concrete, which resulted in a significant reduction in the setting time of the prepared ultra-high-performance concrete. This can be applied to the rapid repair of concrete structures.

Regarding the mechanism of strength formation of cured red mud, scientists generally agree that there are three stages, namely, the early strength formation stage, the strength enhancement stage, and the late strength formation stage. The incorporation of diverse modifying materials exerts a profound influence on the growth of strength in modified red mud at various stages. For instance, the introduction of an early-strengthening agent prolongs the early strength growth stage, whereas the addition of a catalyst accelerates the rate of strength formation (Hao, 2022). The majority of scholars posit that the addition of modified materials, such as cement, lime, and gypsum, and the subsequent hydration reaction that produces calcium hydroxide ($Ca(OH)_2$) and calcium silicate hydrate (C-S-H) gels is the primary factor in strength formation (Zhang et al., 2016). For instance, red mud-based gelling materials have been demonstrated to be effective in stabilizing sodium ions (Na^+) in red mud by forming chemical bonds through adsorption (Yifan et al., 2023). In a study by Luo et al. (Zhongtao et al., 2022), a geopolymer containing more than 50% red mud was used to stabilize chromium present in chromium slag. This stabilization was achieved mainly through calcium–aluminum–silicate–hydrate (C-A-S-H) gels and the physisorption capacity of sodalite. Furthermore, Liu et al. (Yue et al., 2023) demonstrated that the incorporation of red mud facilitated the formation of aluminum-containing phases and elevated the Al/Ca, Si/Ca, and Fe/Ca ratios in the resulting (C-A-S-H) gels. At moderate replacement levels, the reacted red mud enhanced the structure of the binder matrix through its filling effect. This method not only effectively mitigates the various pollution problems arising from red mud storage but also enables the effective utilization of red mud resources. Furthermore, it significantly reduces the energy consumption in the cement and concrete production process, thus providing significant environmental and economic advantages.

The utilization of red mud as a building material has yielded fruitful results. However, the engineering properties of various red muds differ due to differences in processing and origin. Therefore, studying the composition and characteristic structure of red mud can help us to make better use of it. Ahmadi et al. (Hamidreza et al., 2022) investigated the mechanical and structural properties of carbon nanotube geopolymer composites based on metakaolin-red mud. It was demonstrated that the incorporation of red mud had a deleterious impact on the mechanical properties, which is attributable to its low reactivity. Hou et al. (Dongshuai et al., 2021) found that the replacement of cement with red mud increased the plastic viscosity (and shear stress) and reduced the slump flow due to the high specific surface area of the red mud, which limited the application of the red mud in complex shaped constructions, such as tunnels and ultra-high-rise buildings. Liu et al. (Liu R.-X. and Poon C.-S., 2016) observed that the addition of red mud to self-compacting concrete resulted in a reduction in shrinkage. They postulated that this phenomenon may be attributed to the internal curing effect. Furthermore, Liu et al. (Liu R.-x. and Poon C.-S., 2016), in another study, used red mud to replace fly ash in self-compacting mortar mixtures and found that the compressive strength was higher than that of other specimens when the replacement rate of red mud in the mortar mixtures was 50%, which suggests that red mud itself is not very strong, but when red mud

is filled in the material voids, it reacts to produce silicate gels to improve the strength of the material.

In the current published research, the utilization of red mud as a solid waste has received a lot of attention. Many research workers have used other additives for modification to treat red mud. However, there are fewer studies on the influence of multiple factors on modified red mud; especially, the study on the influence of red mud types on the properties of modified red mud is more limited. In this study, orthogonal experiments were conducted to investigate the effects of multiple factors on modified red mud, and a series of microscopic means were used to observe and analyze the samples before and after the modification of red mud, to obtain the mechanism of the action of modified materials on red mud, and to investigate the mechanism of the reaction process of the modified red mud samples at different conservation ages by observing and analyzing the microstructure of the samples.

In this study, we used red mud as the raw material and explored the role of three elements of two ash ratio (ratio of lime to fly ash), two ash content (total lime and fly ash), and red mud types on red mud by the orthogonal test, and got a better modification scheme with better effect by using compaction and compressive properties as indexes. The temperature-shrinkage property of the modified scheme is also evaluated, the composition was analyzed by XRD, the microstructure was fully observed by SEM, and a detailed compositional analysis was carried out on the generated characteristic structure by EDX to reveal the mechanism of strength formation of the modified red mud. This work will help to study the role of multiple influencing factors on modified red mud based on the previous work and have further research on the micro-action mechanism of multi-factor modified red mud.

2 Materials and methods

2.1 Materials

2.1.1 Red mud

The red mud utilized in this study was sourced from two distinct suppliers: Chalco Shandong Co., Ltd (CRM) and Shandong Weiqiao Aluminum and Electric Co., Ltd (SRM). CRM is brownish-brown, lumpy, and readily compressible into powdered solids, with particle sizes ranging from 0.088 to 0.250 mm. SRM is reddish-brown, viscous, with clumping of particles. It lacks large particles and has a particle size range of 0.001–0.100 mm. The morphology of the two types of red mud is illustrated in Figure 1, and the specific physicochemical properties of the two types of red mud are presented in Table 1.

The chemical components of the two red muds were analyzed using X-ray fluorescence spectroscopy (XRF), which revealed that there is not much difference between the constituent elements of the two red muds. Nevertheless, there is a discrepancy in the quantity of each oxide present, with the concentration of SiO_2, CaO, and Na_2O in CRM being higher than that in SRM. The Fe_2O_3 and Al_2O_3 contents of SRM are higher than those of CRM, with the Fe_2O_3 content being approximately one-third higher. This discrepancy may be attributed to the differing geographical origins of the two red muds, with CRM originating from Shandong Province, Zibo City, and SRM from Binzhou City, Shandong Province. The specific composition of the two red muds is shown in Table 2.

2.1.2 Lime

The lime used was tertiary slaked lime, produced by Jiangsu Nanjing Lu Xing Science and Technology Co., Ltd. It was white in color, with a bulk density of 0.95 g/cm^3, a particle size of 0.001–0.002 mm, alkaline in nature, and with the composition and basic physical properties as shown in Table 3.

2.1.3 Fly ash

The fly ash utilized was produced by Jinan Pingyin Innovative Composites Co., Ltd. and exhibited a gray coloration, a density of 2.552 g/cm^3, and a bulk density of 1.122 g/cm^3. Its particle size was 0.001–0.015 mm, and it was alkaline in nature. The composition and basic physical properties are presented in Table 4.

2.1.4 Clay

The clay used in the test was sourced from Binzhou, Shandong Province, and was red clay, yellowish brown, with a particle size of 0.001–0.100 mm. The clay exhibited a particle size distribution with a content of particles smaller than 55 μm of approximately 70% and a content of particles smaller than 10 μm of approximately 45%. The coefficient of inhomogeneity (C_u) was 5.67, whereas the coefficient of curvature (C_c) was 2.52. The plasticity index was 10.8, indicating that the clay in question belongs to the low liquid limit category.

2.2 Preparation of modified red mud

The orthogonal test method is an experimental design method that arranges multi-factor and multi-level tests in a scientific manner and analyses performance indicators by mathematical and statistical methods. In contrast to conventional testing methodologies, the orthogonal test can minimize the number of tests conducted while maintaining the comprehensive nature of the acquired data. The orthogonal test method has been employed extensively in a number of scientific disciplines, including chemistry and medicine. In recent years, research results have emerged on the application of the orthogonal test design method to the field of road engineering. The orthogonal test method is employed in the proportion design of modified red mud, with consideration given to three factors: two ash ratio (factor A), two ash content (factor B), and red mud type (factor C), with two ash ratios of 0.1:1, 0.5:1, and 1.5:1, defined as A1, A2, and A3, respectively; two ash contents of 25%, 50%, and 75%, defined as B1, B2, and B3, respectively; and red mud types, taken as CRM, SRM, 70% CRM, and 30% clay mixes, defined as C1, C2, and C3.

The materials utilized in the tests included CRM, SRM, lime, fly ash, and clay. Prior to commencing the tests, the following treatment was carried out: the temperature of the drying oven was set at 50°C, and all materials were dried for 12 h. The red mud was crushed with a wooden hammer or a wooden mill, and all soil clusters were crushed until they could pass through a 4.75-mm square hole sieve.

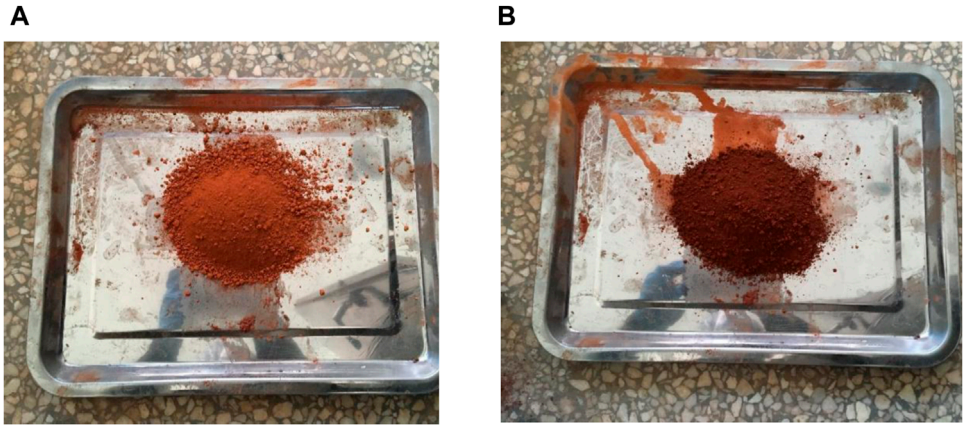

FIGURE 1
Morphology of two types of red mud: **(A)** CRM and **(B)** SRM.

TABLE 1 Physical and chemical properties of red mud.

Pilot project	CRM	SRM
Liquid limit/%	50.9	48.0
Plastic limit/%	44.0	33.4
Plasticity index	6.9	14.6
Natural water content/%	41.4	40.73
PH	12.20	9.28

According to the test protocol, a certain quantity of dried red mud is to be placed on a metal plate. According to the prior calculation, the amount of water is then added to the test material, which is evenly sprayed on the test material. The material is then mixed thoroughly with a sampling shovel until it reaches a uniform state. Finally, the material is loaded into an airtight container. Alternatively, the material can be stored in a plastic pocket in a cool, dry place at room temperature for 12 h. Prior to commencing the test, lime, fly ash, and clay were added to the treated red mud in accordance with the specified proportions (see Table 5), and thoroughly mixed with a small shovel until a homogeneous mixture was achieved. The specimens were then prepared in accordance with the test requirements.

The test procedure was as follows: first, elemental analysis of red mud, lime, fly ash, and clay was carried out by XRF; then, the compaction test was carried out according to the ratios, the optimum ratio was obtained by obtaining the optimum moisture content and the maximum dry density for the unconfined compression test according to the compaction test, and the temperature shrinkage test was carried out according to the optimum ratios. The test pieces crushed in the unconfined compressive strength were collected and pre-treated, and then XRD, SEM, and EDX were performed. The specific flowchart is shown in Figure 2.

2.3 Mechanical test

2.3.1 Compaction test

In accordance with the test procedures and specifications outlined in the "Test method of soils for highway engineering" (JTG E40-2007) ("Test method of soils for), the II.1 heavy-duty compaction test method was employed to treat the red mud and modified red mud materials.

The instrument utilized was an electric compaction device. Prior to each sample undergoing compaction, the moisture content was measured. Following the completion of the compaction process, the dry density was measured. Five sets of data were fitted with water content as the x-axis and dry density as the y-axis in order to obtain the optimum water content and maximum dry density, which are indicative of compaction properties.

2.3.2 Unconfined compression test

The compaction of the unconfined compressive strength test piece was controlled according to 96%, and the test piece was molded by the static compression method for 1 min, and then unloaded; after molding, the test piece is demolded, and then it was placed in a standard curing box with the temperature of 14°C ± 1°C and relative humidity ≥90% after being loaded with an open mouth in a ziplock bag for curing.

The instrument used was a fully automatic pavement material strength tester, and the loading rate of the test piece was carried out at an axial strain rate of 0.12 mm–0.36 mm per minute. When the force value reaches its peak value, it is necessary to continue to shear 3–5 per cent of the strain value before the test can be stopped.

2.3.3 Temperature shrinkage test

Before the temperature shrinkage test begins, the test piece is dried in an oven at a temperature of 100°C ± 5°C until the mass of the specimen no longer changes. At this point, the test piece is removed from the oven and brought to room temperature. The temperature shrinkage test is then carried out.

The test apparatus for the temperature shrinkage test is a high and low temperature alternating test chamber. The test-piece is

TABLE 2 Chemical composition of red mud.

Type	Chemical content/%								
	SiO_2	Fe_2O_3	Al_2O_3	CaO	MgO	TiO_2	Na_2O	CO_2	Loss
CRM	14.03	24.87	17.37	9.56	0.31	4.87	6.21	20.72	2.06
SRM	10.78	33.16	22.25	2.90	0.44	4.91	5.84	17.77	1.95

TABLE 3 Physical and chemical properties of lime.

Target		Measured value
Content of effective CaO and MgO/%		55.23
Water content/%		29.34
Fineness	Screen residue from 0.60 mm square hole sieve/%	18.9
	Screen residue from 0.15 mm square hole sieve/%	17.6
Magnesium oxide content/%		1.1

TABLE 4 Physical and chemical properties of fly ash.

Target	Measured value
Content of SiO_2, Al_2O_3, and Fe_2O_3/%	80.20
Loss on ignition/%	7.90
Passing rate of 0.3 mm square hole sieve/%	98.30
Passing rate of 0.075 mm square hole sieve/%	81.59
Water content of fly ash/%	0.75

mounted on the shrinkage tester and put into the test chamber, where the temperature control is from the high temperature, to reach the set temperature after holding for 3 h, the rate of change of temperature is set to 0.5°C /min, according to the rate of this cooling rate step by step.

2.4 Composition analysis test

2.4.1 X-ray fluorescence spectroscopy analysis (XRF)

The XRF test was carried out using a fully automatic scanning X-ray fluorescence spectrometer, Rigaku ZSX Primus II, Japan, for rapid qualitative and quantitative analyses of elements from 6C to 92U. The detection range of the elements was 0.0001%–100%.

2.4.2 X-ray diffraction analysis (XRD)

Before XRD, SEM, and EDX, the test pieces need to be pre-treated. The test pieces crushed in the strength test were collected according to ratios, ground with a mortar and pestle, soaked in anhydrous ethanol for 48 h to terminate hydration, then dried at 40°C and passed through an 800-mesh sieve, and then packed into specimen bottles according to different ratios and ages, and set aside for the tests to be carried out within 2 working days.

The XRD tests were carried out using a Panalytical Empyrean X-ray diffractometer from the Netherlands, with operating conditions of voltage 60 kV, current 60 mA, Cu target, wavelength 0.15418 nm, scanning angle 2θ of 10°–90° in steps of 0.0001°, and PIXcel3D omni-matrix detector, with the analytical database version ICDD PDF-4 2014.

2.5 Microstructure analysis test

2.5.1 Scanning electron microscopy (SEM)

The SEM tests were performed using a German Zeiss SUPRA™ 55 thermal field emission scanning electron microscope with an accelerating voltage of 0.1–30 kV and resolutions of 1.0nm@15kV, 1.7nm@1kV, and 4.0nm@0.1kV, and 2000X, 5,000X, and 20,000X magnification phases were taken from a typical position selected for each sample.

2.5.2 Energy-dispersive X-ray spectroscopy (EDX)

The energy spectrum analysis was carried out with the help of an X-ray energy spectrometer in SEM configuration. For the analysis, the position is first determined by SEM, then the lens is switched, and then the point is taken for that position. The range of elements that can be analyzed is from 4Be to 94Pu using the X-ray electrocooled energy spectrometer that comes with the scanning electron microscope.

3 Results and discussion

3.1 Evaluation of physical properties of modified red mud

3.1.1 Compaction characteristics

From Figure 3, it was found that the optimal moisture content of modified red mud is between 31% and 37%, and for the size of optimal moisture content of the compaction test, red mud types are the most important influencing factor, and two ash content and two ash ratio have a weaker influence.

10.3389/fmats.2024.1461198

TABLE 5 Modified red mud treatment program.

Number	Lime/%	Fly ash/%	Red mud/%	Clay/%	Two ash ratio (A)	Two ash content/% (B)	Red mud types (C)
1	2.3	22.7	75	0	0.1:1	25	CRM
2	4.6	45.4	50	0	0.1:1	50	SRM
3	6.8	68.2	17.5	7.5	0.1:1	75	CRM
4	8.3	16.7	75	0	0.5:1	25	SRM
5	16.7	33.3	35	15	0.5:1	50	CRM
6	25	50	25	0	0.5:1	75	CRM
7	15	10	52.5	22.5	1.5:1	25	CRM
8	30	20	50	0	1.5:1	50	CRM
9	45	30	25	0	1.5:1	75	SRM

That is, in the test results, the order of the factors is C > B > A. For factor A of the two ash ratio, the order of the levels is A3 > A1 > A2, and A3 is the optimal level among the three indexes, and A2 is the most inferior level. For two ash content factor B, its level is in the following order: B1 > B2 > B3, B1 is the optimal level among the three indicators, and B3 is the most inferior level. For red mud type factor C, the level of the order of precedence is as follows: C1 > C3 > C2; in the three indicators, C1 is the optimal level and C2 is the most inferior level; that is, A3B1C1 has the highest optimal moisture content and A2B3C2 has the lowest optimal moisture content.

As seen in Figure 4, the maximum dry density of modified red mud is between 1.29 and 1.43 g/cm^3. For the size of the maximum dry density of the compaction test, the amount of two ash content is the most important influencing factor, the two ash ratio is the second most important influencing factor, and the influence of the red mud types is between the two.

That is, in the test results, the order of the factors is B > C > A. For two ash ratio factor A, the order of the level is A2 > A1 > A3, and A1 is the optimal level among the three indexes, and A3 is the most inferior level. For two ash content factor B, the order of their level is B1 > B2 > B3 among the three indicators, B1 is the optimal level, and B3 is the lowest level. For red mud type factor C, the level of the order of precedence is as follows: C2 > C3 > C1; in the three indicators, C2 is the optimal level and C1 is the least level. In summary, A2B1C2 has the highest maximum dry density and A3B3C1 has the lowest maximum dry density.

The results demonstrate that red mud type (factor C) has a significant impact on both optimal moisture content and maximum dry density, as illustrated in the preceding figure. It can be observed that different red muds contain varying proportions of components, with the proportions of different oxides also affecting the optimal water content and the maximum dry density to a considerable extent. The two ash content (factor B) has a significant effect on the maximum dry density and the maximum dry density is affected to a greater extent than the optimal moisture content, whereas the effect of the two ash ratio (factor A) on both optimal moisture content and maximum dry density is relatively minor. The addition of clay to red mud has a noticeable impact on both the optimal moisture content and the maximum dry density, as evidenced by the reduction in the optimal moisture content and the increase in the maximum dry density with the addition of 30% clay. When red mud is employed for roadbed filling, the ratio of compaction density and water content suitable for local working conditions can be obtained by the addition of clay.

3.1.2 Strength characteristics

The unconfined compressive strength test is a strength test in which the specimen is subjected to conditions that are not laterally confined. As illustrated in Figure 5, the three influencing factors exert varying effects on test pieces of the same age. Nevertheless, the trend of the three influencing factors is consistent across the three ages: 7, 28, and 90 d.

With the increase of lime proportion in the two ash ratio (i.e., the amount of lime increased), the strength of all ages increased, of which the strength of the 28 d age was the most significantly affected by the two ash ratio. Liu et al. (Juanhong et al., 2020) found that the lime admixture promoted the fly ash hydration

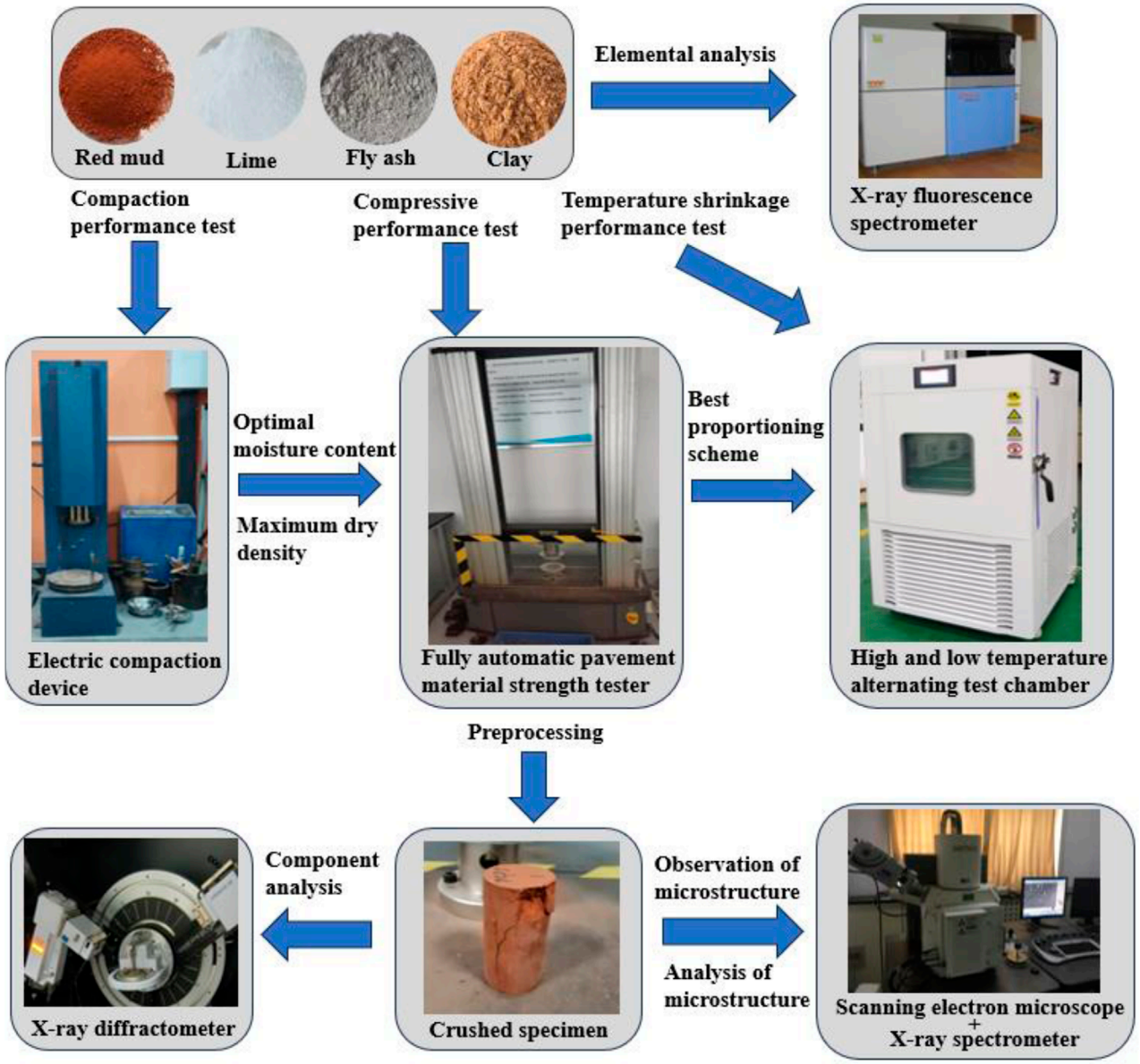

FIGURE 2
Test flowchart.

reaction and accelerated the hydration process of red mud–fly ash cementitious materials, which just confirmed the test results. With the increase of the two ash content, the strength of all ages showed the law of increasing and then decreasing, the strength of the 7 d age was least affected by the factor, and the strength of the 28 and 90 d age was equally affected by it, which indicates that this factor mainly affects the medium- and long-term strength; changing the red mud type found that the strength of C2 is smaller than those of C1 and C3 under the same age, and the strength of C3 is the highest under the age of 7 d and 28 d, but at the age of 90 d, the strength of C1 has been significantly higher than that of C3.

As can be seen from Figure 5, for the test pieces at the age of 7 and 90 d, the two ash ratio is their most significant influencing factor, and the effects of red mud type and two ash content are weaker, but the optimal levels of their influencing factors are different, which are A3B2C3 and A3B2C1, respectively; for the test pieces at the age of 28 d, the red mud type is its most significant influencing factor, but the effect of the two ash ratios on this age is also belonging to a stronger level, and the optimum level of the influencing factor is the same as that of the 7 d age, which is A3B2C3.

In the test results of three ages, the number of occurrences of the most important factors is as follows: 2 times A, 0 times B, and 1 time C; the number of occurrences of the most important factors is as follows: 0 times A, 3 times B, and 0 times C. Therefore, it is determined that factor A of the two ash ratios is the most important influencing factor, factor

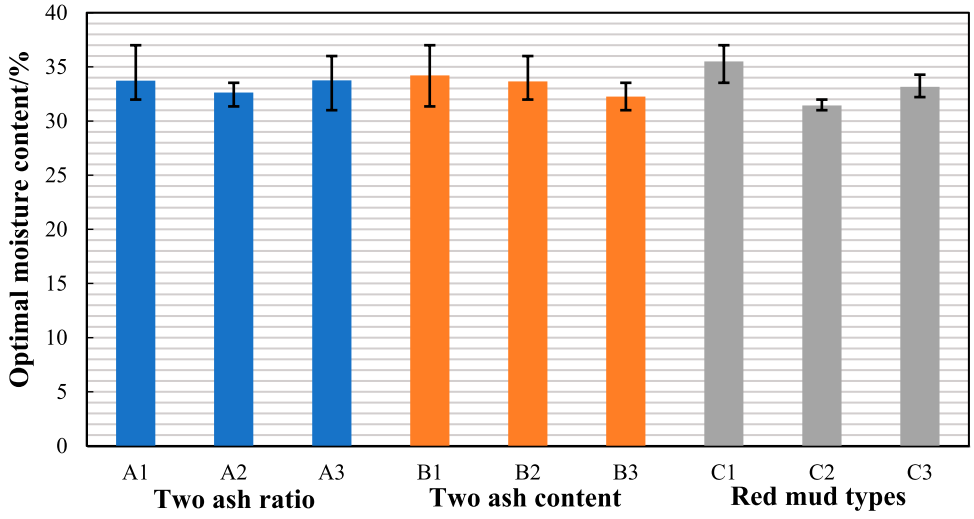

FIGURE 3
Optimal moisture content *versus* factor histogram.

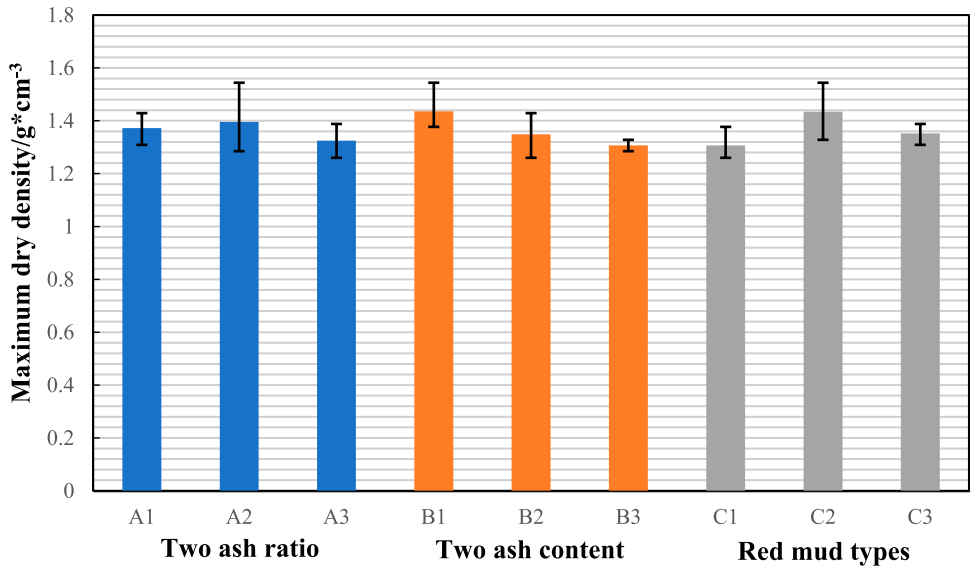

FIGURE 4
Maximum dry density *versus* factor histogram.

C of the red mud type is the secondary influencing factor, and factor B of the two ash content is the most secondary influencing factor.

For two ash ratio factor A, the number of times its optimal level occurs is as follows: 0 times A1, 0 times A2, and 3 times A3; the number of times its least level occurs is as follows: 3 times A1, 0 times A2, and 0 times A3. A3 is the optimal level among the three indexes, so it can be determined that its optimal level is A3. For two ash content factor B, the total number of occurrences of the optimal level is as follows: 0 times B1, 3 times B2, and 0 times B3; the number of occurrences of its least level is as follows: 1 times B1, 0 times B2, and 2 times B3. B2 is the optimal level in all the three indexes, so it can be determined that its optimal level is B2. For red mud type factor C, the number of times its optimal level occurs is as follows: 1 times C1, 0 times C2, and 2 times C3; the number of times its least level occurs is as follows: 0 times C1, 3 times C2, and 0 times C3. C3 occurs twice the optimal level among the three indexes, so it can be determined that its optimal level is C3.

In conclusion, the optimal three-factor optimization scheme for the base layer of two ash stabilized red mud pavement is A3B2C3. However, the long-term performance of the road construction is of paramount importance. A comparison of C3 and C1 reveals that there is no significant difference in strength at the age of 90

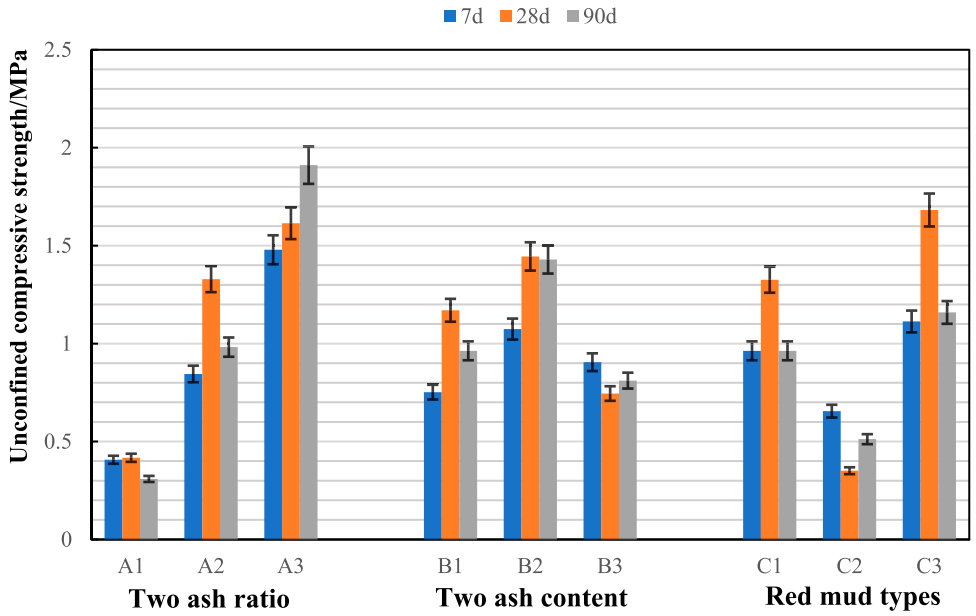

FIGURE 5
Unconfined compressive strength *versus* factor histogram.

days. Furthermore, the long-lasting red mud can provide a higher strength than similar particle size powder clay, thus justifying an adjustment to C1. This not only meets the long-term strength requirements of the pavement but also improves the resource utilization of the red mud. Consequently, C3 can be adjusted to C1, which not only fulfill the long-term strength requirements of the pavement but also enhances the resource utilization rate of red mud. Furthermore, the optimal solution for practical application can be proposed as A3B2C1, that is, lime: fly ash: CRM = 30:20:50.

3.1.3 Temperature shrinkage characteristics

The application of inorganic binding material stabilization to the pavement base layer, in winter, due to the temperature difference will produce temperature stress. This is manifested by a surface temperature that is lower than the internal temperature, and there is tensile stress at the top of the grass-root level, and the combination of tensile stress at the bottom of the grass-root level with the driving load will lead to cracking of the structural layer and other diseases. Temperature shrinkage performance refers to the performance of the inorganic binding material stabilization material shrinking in size after cooling down when the ambient temperature decreases. The ratios for the temperature shrinkage test were chosen to be the two ratios with the highest unconfined compressive strength. A3B2C3 (ratio 3) and A3B2C1 (ratio 4) were the best combinations for the orthogonal test, with the former having a better early strength, and the latter having a higher long-term strength. The two red mud raw materials, namely, CRM (ratio 1) and SRM (ratio 2), were also tested as control.

The softening and disintegration of the SRM (ratio 2) test pieces during the water immersion stage indicated that the water stability properties of this red mud raw material were not sufficient to meet the required standards. Consequently, the test results were analyzed only for the remaining three ratios. The temperature shrinkage properties of an inorganic binding material are characterized by the temperature shrinkage coefficient, which is the coefficient of shrinkage of the material at a constant moisture content, when the temperature is decreased. A negative power function was used to fit the score, but as the temperature starting point is negative, all data were shifted by 10 temperature units in the positive direction along the *x*-axis for the fitting calculation, and the fitting results are shown in Figure 6, which shows that the three fitted curves, all with $R^2 > R^2_{0.05}(3) = 0.8783$, indicate that the regression equation is significant at the confidence level of $\alpha = 0.05$. This indicates that the temperature shrinkage coefficients of the three ratios of red mud materials, in the double logarithmic coordinate system, show a linear change; that is, as the temperature increases, the temperature shrinkage coefficient decreases, and the lower the temperature, the greater the temperature shrinkage coefficient.

The temperature shrinkage coefficient is larger in the lower temperature zone (less than 10°C) for A3B2C3 (ratio 3) and A3B2C1 (ratio 4), and the rate of change is larger with decreasing temperature. In the higher temperature zone (greater than 10°C), the temperature shrinkage coefficient is smaller, and with the decrease of temperature, the rate of increase of temperature shrinkage coefficient is smaller than that in the low-temperature low zone, for CRM (ratio 1), and the temperature lodging coefficient in the high-temperature high zone is almost unchanged.

Overall, the temperature shrinkage coefficients of the three ratios are in accordance with the engineering requirements, and the temperature shrinkage coefficients of red mud obtained by You through the study of red mud-based cementitious materials are better (Hao, 2023), which is consistent with the test results. The temperature shrinkage coefficients of A3B2C3 (ratio 3) and A3B2C1 (ratio 4) are higher than that of CRM (ratio 1), and the temperature shrinkage change of the modified red mud is greater than that of the

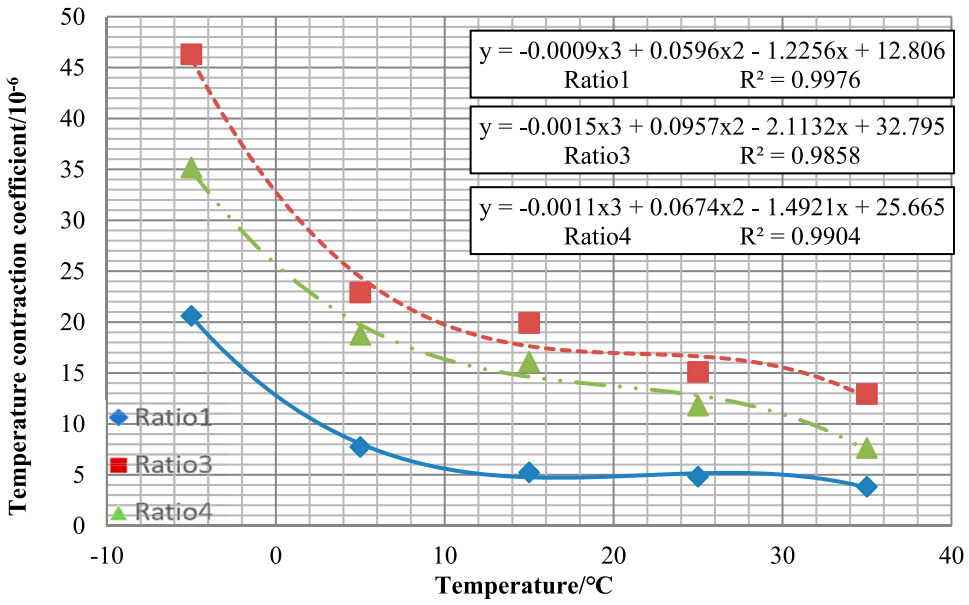

FIGURE 6
Fitting curve of temperature shrinkage coefficient *versus* temperature.

red mud, which suggests that the addition of the modified materials will make the red mud's temperature shrinkage coefficient increase. The temperature shrinkage coefficient of A3B2C3 (ratio 3) is higher than that of A3B2C1 (ratio 4), which indicates that adding clay to red mud will increase its temperature shrinkage coefficient, and the temperature shrinkage coefficient increases by about 30.9% by replacing 30% of the red mud with clay in the ratio, so it is possible to flexibly decide whether it is necessary to add clay or not according to the specific working conditions during construction. Temperature shrinkage characteristics alone, in the temperature difference of the region, can be used in modified red mud filler, whereas pure red mud as filler application range is more extensive.

3.2 Compositional analysis of modified red mud

3.2.1 XRD analysis

The XRD analysis of the CRM raw material is shown in Figure 7, from which it can be seen that the included material phases are hematite (Fe_2O_3), calcite ($CaCO_3$), perovskite ($CaTiO_3$), boehmite (γ-AlO(OH)), quartz (SiO_2), hydrous calcareous zeolite ($CaAl_2Si_2O_8{\cdot}4(H_2O)$), and goethite (α-FeO(OH)), magnetite (γ-Fe_2O_3), and magnesium chlorite ($(Mg_2Al)[SiAlO_5](OH)_4$).

Iron compounds, including hematite (Fe_2O_3), goethite (α-FeO(OH)), and magnetite (γ-Fe_2O_3), are produced either by oxidation of red mud after exposure to air or by dehydration of water-bearing iron-oxidized minerals during deposition of the ore, and the types of compounds produced are highly dependent on the composition of the ore (Zhang et al., 2024). Goethite (α-FeO(OH)) and boehmite (γ-AlO(OH)) have some hydration capacity and CRM contains some calcite ($CaCO_3$) to provide strength.

The XRD analysis of the raw material of SRM is shown in Figure 8, which contains the physical phases of hematite (Fe_2O_3), calcite ($CaCO_3$), perovskite ($CaTiO_3$), boehmite (γ-AlO(OH)), pyrite (FeS_2), gibbsite ($Al(OH)_3$), and garnet ($Ca_3TiFeSi_3O_{12}$).

Comparison of CRM reveals that the physical phases of the two are slightly different, which is a normal phenomenon due to the different mineral compositions in different aluminum ores. SRM contains both boehmite (γ-AlO(OH)) and the hydration product of boehmite (γ-AlO(OH)) and gibbsite ($Al(OH)_3$), which represents the possibility that some hydration reaction may have taken place in it. In addition to the composition of the physical phases, the relative intensities of the same phases in the two red muds are very different. As can be seen from the peak heights and half-peak widths, hematite (Fe_2O_3), the major oxide of iron, is significantly more crystalline in SRM than in CRM, as can be seen from the XRF of CRM and SRM, where the hematite (Fe_2O_3) content of SRM is one-third higher than that of CRM, suggesting that the degree of crystallization is higher in SRM.

The modified red mud curing body samples with ratio A3B2C3 were selected, and the samples maintained for 7 and 28 d were prepared and tested, respectively, and the X-diffraction analysis graphs are shown in Figures 9, 10.

From Figures 9, 10, it can be seen that the mineral composition of red mud underwent a significant change following the addition of lime and fly ash, indicating the existence of a chemical reaction occurred within the mixture. In Figure 8, the diffraction peaks of the phases of acicular goethite (α-FeO(OH)), magnetite (γ-Fe_2O_3), boehmite (γ-AlO(OH)), and magnesium chlorite ($(Mg_2Al)[SiAlO_5](OH)_4$) have disappeared while new substances such as tricalcium aluminate ($Ca_3Al_2O_6$) and calcium sulphoaluminate ($Ca_4Al_6O_{12}SO_4$) appeared, suggesting that substances such as acicular ferrite are involved in the hydration reaction between the solidifying agent and the

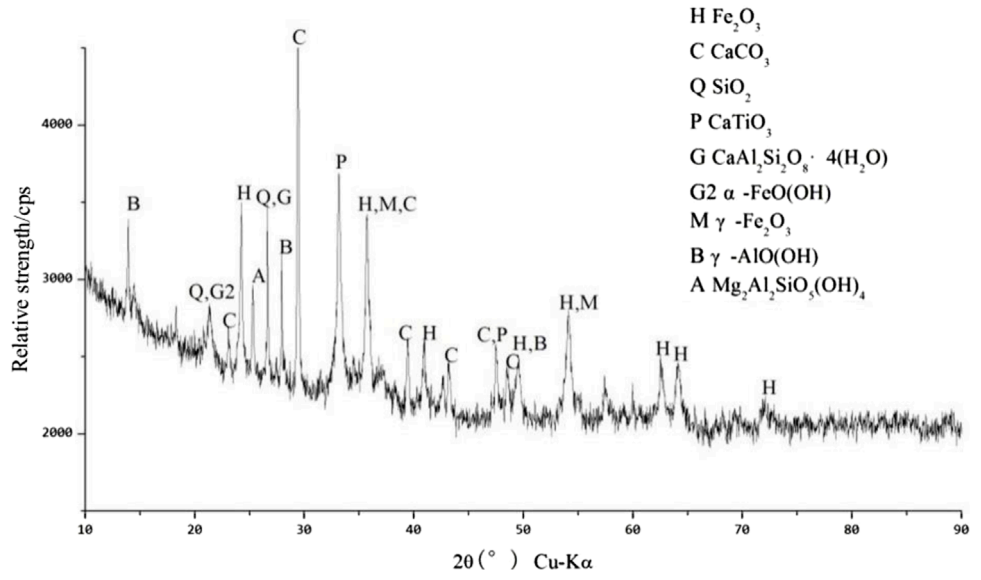

FIGURE 7
X-ray diffraction analysis of CRM.

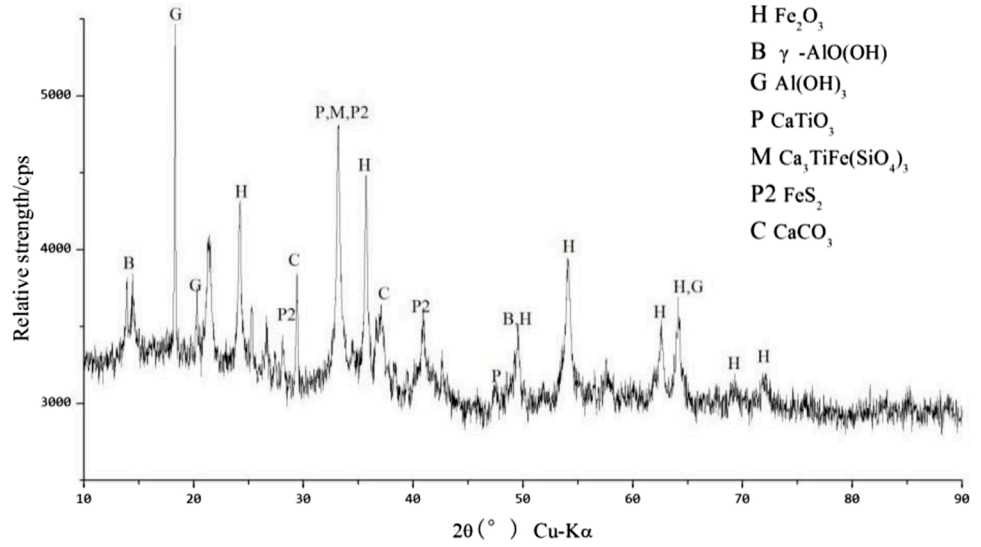

FIGURE 8
X-ray diffraction analysis of SRM.

red mud raw material, resulting in the generation of new crystalline minerals (Jiaolong et al., 2017). On the other hand, hematite (Fe_2O_3), calcite ($CaCO_3$), quartz (SiO_2), perovskite ($CaTiO_3$), and hydrous calcareous zeolite ($CaAl_2Si_2O_8{\cdot}4(H_2O)$) can be found in both the raw and cured red mud, suggesting that the reaction may not have taken place or may have been incomplete. There is also a possibility that after the generation of red mud, due to the NaOH and water contained in it, some hydration reaction may have occurred in the process of stockpiling, generating several of the above substances.

Comparing the X-ray diffraction patterns of red mud before and after curing in Figures 9, 10, it can be seen that the diffraction peaks do not differ much in each position, but the diffraction intensity is weakened and diffuse X-ray peaks appear, indicating that the hydration products are mainly some amorphous aluminosilicates. The physical phase compositions of the samples of different conservation ages were similar, but some new crystalline phases, such as dicalcium silicate ($Ca_2(SiO_4)$), were also detected in the sample of 28 d age. For the amorphous material produced by hydration, the most likely substance it contains is

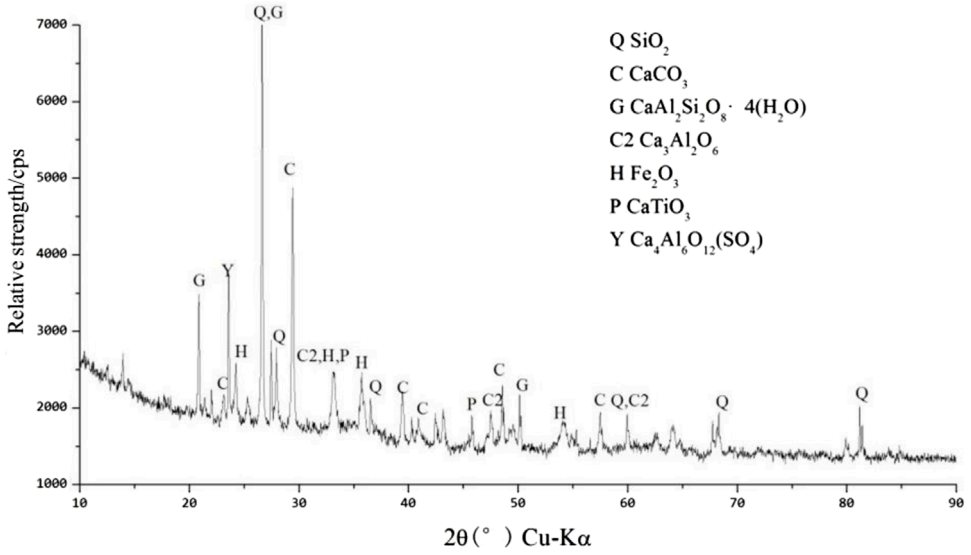

FIGURE 9
X-ray diffraction analysis of test pieces maintained for 7 d.

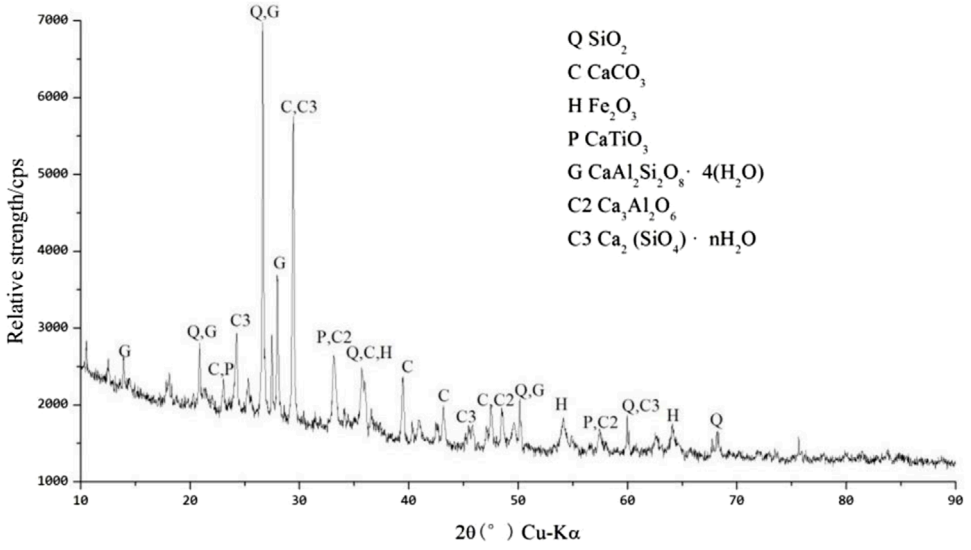

FIGURE 10
X-ray diffraction analysis of test pieces maintained for 28 d.

hydrated calcium silicate ($CaO{\cdot}SiO_2{\cdot}H_2O$, C-S-H), which is mostly found in cement hydration reaction products (Xiangqun et al., 2018), and is contained in red mud, including calcite ($CaCO_3$) and hydrous calcareous zeolite ($CaAl_2Si_2O_8{\cdot}4(H_2O)$), tricalcium aluminates ($Ca_3Al_2O_6$), and dicalcium silicate ($Ca_2(SiO_4)$). The composition of the cured Bayer method red mud is similar to that of aluminate cement, which suggests that it belongs to the category of water-hardening cementitious materials. It may have the following advantages: high early strength, a certain resistance to the corrosive effect of sulfate and heat resistance, and the relative long-term strength of the growth of a slower trend (Yuxu et al., 2024).

3.3 Microstructure analysis of modified red mud

3.3.1 SEM analysis

The use of SEM and EDX enabled the observation of the effect produced by the reaction at the nanoscale and micro level. First, the microstructures of CRM and SRM were observed. Subsequently, the modified red mud with an A3B2C3 ratio of the optimal modification scheme was selected as the main research object to analyze the microstructure of modified red mud, which was divided into two groups of modified red mud with 7dA3B2C3 ratio and 28dA3B2C3 ratio to form the time comparison, and formed the comparison

10.3389/fmats.2024.1461198

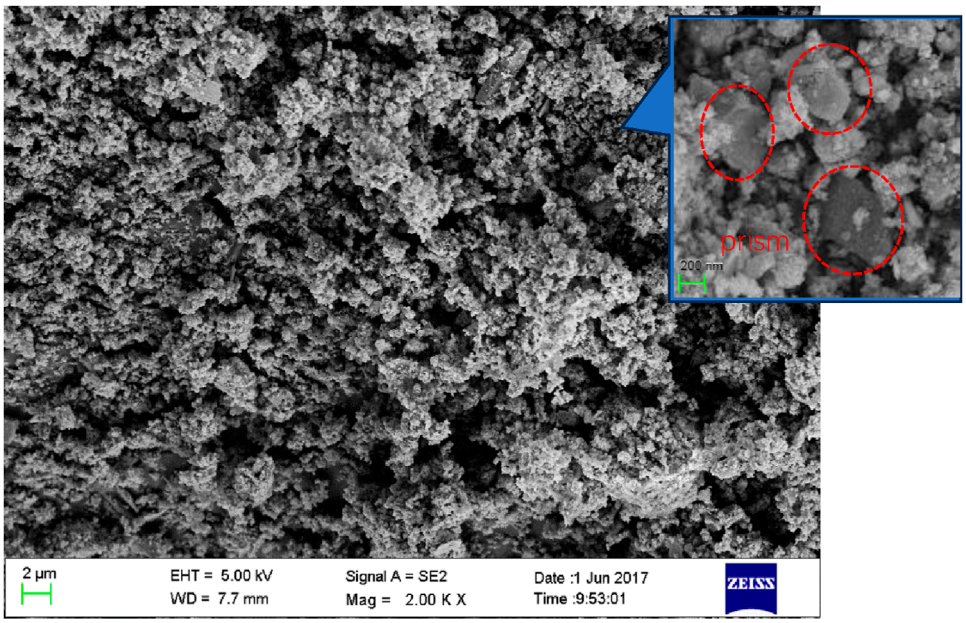

FIGURE 11
Scanning electron microscopy analysis image of CRM 2000X.

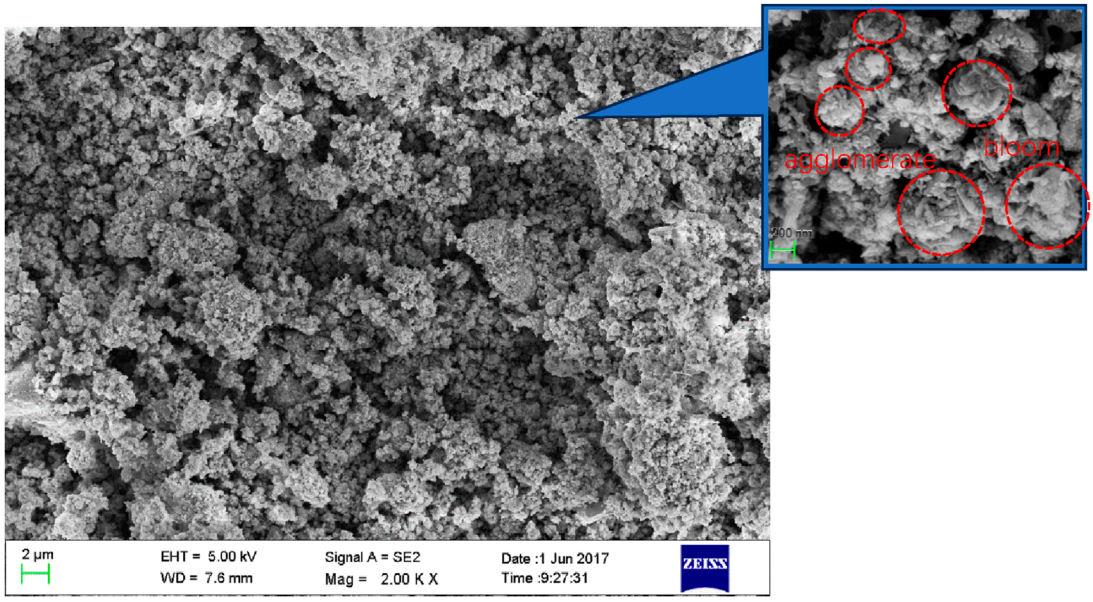

FIGURE 12
Scanning electron microscopic analysis of SRM 2000X.

with the red mud raw materials before and after the reaction, with the magnifications of 2000X, 5000X, and 200,00X, and the typical structure was selected to stay in the picture.

As can be seen from Figure 11, the surface particles of the CRM are characterized by a rough and porous structure, which contributes to the low mechanical strength of the original red mud. Comparing Figures 11, 12, it can be found that there are some differences in the microstructure of CRM and SRM.

First, there is a difference in the particle composition of the two kinds of red mud: there are many prismatic, lamellar, and layered structures in CRM, which may be Ca- and Si-bearing minerals, which are rare in SRM, and it can be found that the particles in SRM are mostly agglomerates and blooms, which may be Fe-, Al-, and Na-bearing minerals; second, there is a difference in the size of particles of the two kinds of red mud: as shown in Figure 11, the diameters of these structures in the CRM range from 200 nm to 1–2 µm, and

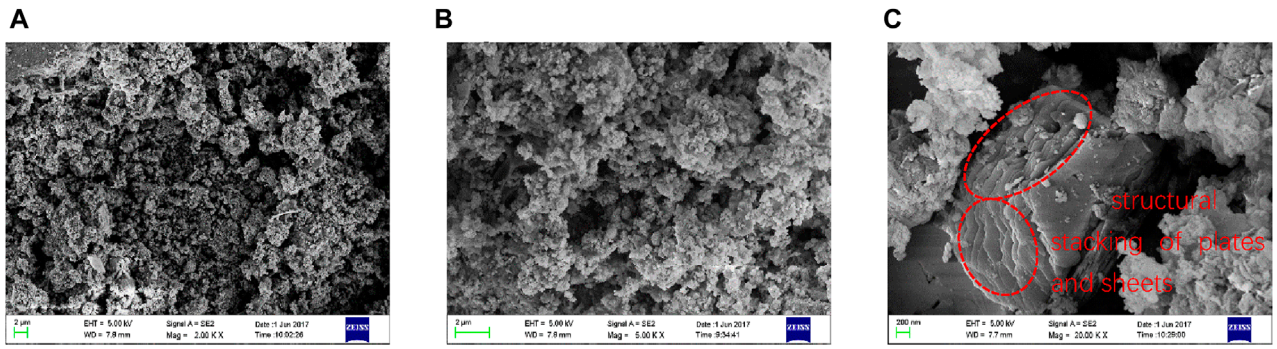

FIGURE 13
Scanning electron microscopy analysis of 7 d modified red mud: **(A)** 2000X, **(B)** 5,000X, and **(C)** 200,00X.

as shown in Figure 12, the particle size of SRM is larger than that of the former, which can reach 4 μm. However, there are some common features, such as the same looseness and many cavities, which should also be the reason for its low strength.

As shown in Figure 13, the structure of the CRM underwent a transformation following the incorporation of lime and fly ash for curing.

As illustrated in Figure 13A, the particle size of certain large particles increased to approximately 5–10 μm. This alteration resulted in a notable reduction in the voids on the surface of the particles, thereby enhancing the overall structural coherence. Second, it can be observed that the surface of the structure became smoother and exhibited a denser state. Not only did the number of plate-like and lamellar structures increase but also these intricately shaped configurations began to intertwine with each other, forming more layered and intricate network-like organizations, as shown in Figure 13C, and the intertwining of these structures may have helped to improve the strength and durability of the material. Finally, there was an increase in prismatic dark-colored materials; these structures have smooth surfaces and more regular shapes and were present in small amounts in the original red mud, but their density increased significantly after curing (Jingfu et al., 2007). It is inferred that they may become an important part of the structure of the reinforcing material. From this, we can see that the two ash-curing treatments greatly enriched the microstructure of CRM and enhanced its properties.

A comparison of Figures 13B, 14B reveals that the distance between the particles of the modified cured red mud is reduced and the structure becomes denser with an increase in maintenance time. As illustrated in Figure 14A, some of the larger particles have reached a size of 20–30 μm, the surface is flat, and the large voids are filled by newly generated crystalline and amorphous materials. The lamellar, platelet, and prismatic materials are further developed, and they are connected by filamentous and reticulated materials between the structures, which enhances the structural strength, as shown in Figure 14C (Gaole et al., 2024).

This mesh-like material, which is widely present inside the structure, is a hydrated calcium silicate gel (C-S-H) generated by hydration (Yang and Guozhong, 2008), which acts like a glue to join the bulk structure together, resulting in a much higher mechanical strength of the cured body. It can be seen that prismatic and reticular substances play an important role in the curing process of the Bayer method red mud. This prismatic material may be calcium hydroxide ($Ca(OH)_2$), tricalcium aluminates ($Ca_3Al_2O_6$), or calcium carbonate ($CaCO_3$), and its actual composition needs to be investigated by energy spectrum analysis.

3.3.2 EDX analysis

The elemental composition and content of the structure of the prismatic crystalline material was analyzed by X-ray energy spectrometry (EDX) analysis of the typical structure of the A3B2C3 ratio, as shown in Figure 15.

From Figure 15, it was found that the atomic ratio of aluminum to oxygen is about 1:2 and that it contains almost no common elements other than hydrogen (hydrogen could not be detected by the energy spectrum analysis), so it can be guessed that this substance is most likely to be boehmite (γ-AlO(OH)). From the above, boehmite (γ-AlO(OH)) and goethite (α-FeO(OH)) were consumed during the hydration reaction, and this is supported by microscopic analyses. It can be reasonably assumed that the bulk crystalline materials are quartz (SiO_2), as shown in Figure 16, which has an oxygen-to-silicon atomic ratio close to 2:1. In addition, the presence of quartz (SiO_2) in CRM can be proven by performing XRD (Shangjiefu et al., 2023).

In summary, after adding lime and fly ash, the strength of the solidified body has been greatly improved through a series of hydration reactions. First, boehmite (γ-AlO(OH)) and goethite (α-FeO(OH)) participate in a series of reactions to generate crystalline substances such as tricalcium aluminate ($Ca_3Al_2O_6$), which is the basis for the early strength formation of red mud. With the extension of maintenance time, some amorphous substances are generated. This network, filamentous, and fibrous substances encapsulate, fill, and bond structures with certain strengths such as calcium carbonate ($CaCO_3$), tricalcium aluminate ($Ca_3Al_2O_6$), and garnet ($Ca_3TiFeSi_3O_{12}$), greatly improving the strength of the solidified structure. The main amorphous substance is most likely the hydrated calcium silicate gel ($CaO{\cdot}SiO_2{\cdot}H_2O$, C-S-H). From the reaction product point of view, if a large number of amorphous gel substances that can be wrapped

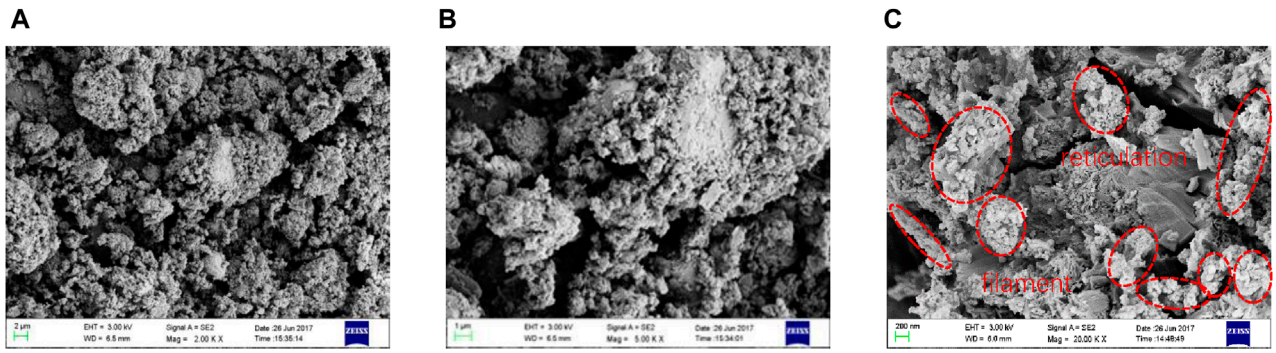

FIGURE 14
Scanning electron microscopy analysis of 28 d modified red mud: **(A)** 2000X, **(B)** 5,000X, and **(C)** 200,00X.

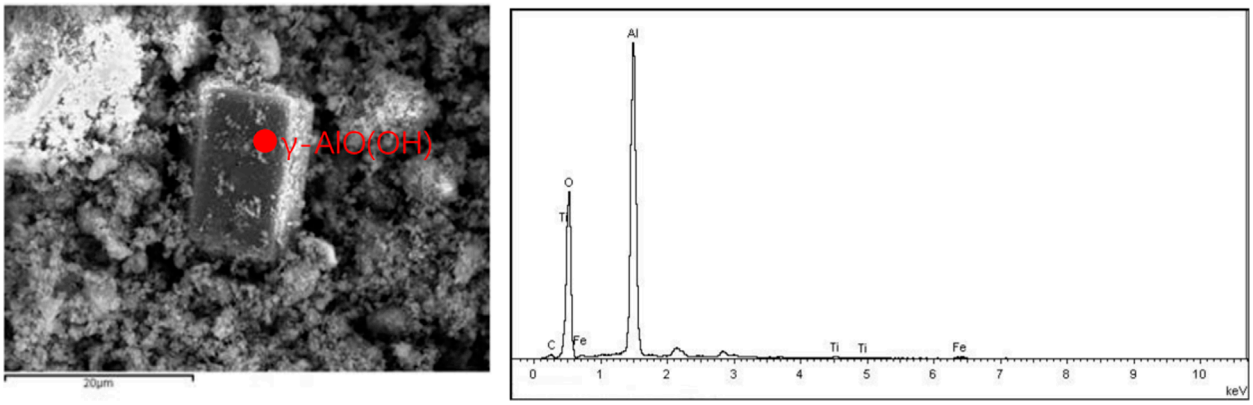

FIGURE 15
EDX analysis of prismatic crystalline materials.

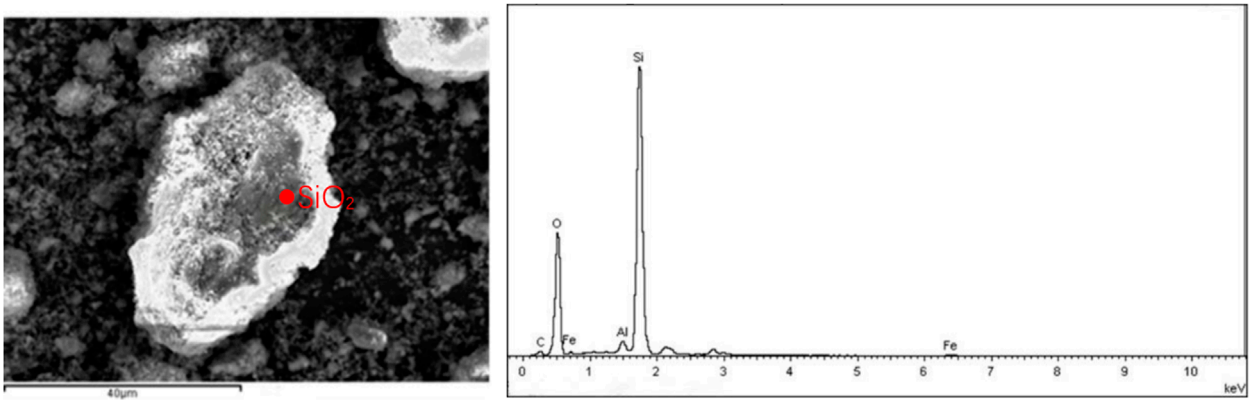

FIGURE 16
EDX analysis of bulk crystalline materials.

and filled are not generated, it is impossible to have strong mechanical strength in terms of the loose porous structure of red mud itself. The main reason for the difference in the strength of test pieces with different ratios and different ages is the difference in the amount of amorphous gel material generated by the reaction.

4 Conclusion and prospects

4.1 Conclusion

In order to study the effects of two ash ratio, two ash content, and red mud types on the compaction and compressive properties of red mud, the effects of factors on red mud were quantified through orthogonal tests, and a ratio scheme with better results was obtained. Temperature shrinkage characteristics, microstructure, and strength formation mechanism of modified red mud were also investigated by means of the temperature shrinkage test and microanalysis. The main conclusions are as follows:

(1) Two ash ratio, two ash content, and red mud types all affect the compaction properties of modified red mud, in which the red mud types have a significant effect on both the optimum water content and the maximum dry density; two ash content has a significant effect on the maximum dry density, but a smaller effect on the optimum water content; and the two ash ratio has a smaller effect on both the optimum water content and the maximum dry density.

(2) The compressive properties of modified red mud are also affected by the two ash ratio, two ash content, and red mud types, as well as the age of maintenance. For the unconfined compressive strength at the age of 7 d, two ash ratios are the most important influencing factors; for the strength at the age of 28 d, red mud types are the most important influencing factors; for the strength at the age of 90 d, two ash ratios are the most important influencing factors. As the proportion of lime in the two ash ratio increases, the strength at all ages increases; as the two ash content increases, the strength at all ages shows a pattern of increasing and then decreasing, and the strength of SRM is smaller than that of CRM, SRM, and clay mixes under the stabilization of two ash. Considering that the results of the long age test are more stable and less affected by the test error, the optimal ratio is A3B2C1, that is, lime: fly ash: CRM = 30:20:50 for the strength at the age of 90 d.

(3) The average temperature shrinkage coefficient of red mud and stabilized red mud in the range of 40°C ~ −10°C is between 8.45 × 10–23.44 × 10%, which can meet the general engineering needs. As the temperature decreases, the temperature shrinkage deformation and temperature shrinkage coefficient of red mud and stabilized red mud both increase gradually, with a slower increase in the interval of 40°C–10°C and a faster increase in the interval of 10°C ~ −10°C. The temperature shrinkage coefficient of stabilized red mud is poorer than that of raw materials, and the addition of clay to red mud can improve the temperature shrinkage coefficient.

(4) After the addition of lime and fly ash, the strength of the cured body was greatly improved after a series of hydration reactions. First, boehmite (γ-AlO(OH)) and goethite (α-FeO(OH)) were involved in a series of reactions to generate crystalline substances such as tricalcium aluminate($Ca_3Al_2O_6$), which was the basis of the early strength of red mud. With the prolongation of the maintenance time, some amorphous substances are generated, and these reticulated, filamentary, and fibrous substances wrap, fill, and cement the structure with certain strength such as calcium carbonate ($CaCO_3$), tricalcium aluminate ($Ca_3Al_2O_6$), and garnet ($Ca_3TiFeSi_3O_{12}$) so that the strength of the structure of the curing body is greatly improved.

In summary, this study obtained a three-factor modified red mud evaluation system and derived an optimal ratio, and its temperature shrinkage characteristics were also studied, which is of guiding significance to engineering practice. In addition, through the means of microanalysis, the strength formation process of modified red mud and the substances that produce strength were obtained, which is complementary to the study of the action mechanism of modified red mud.

4.2 Prospects and limitations

(1) For the utilization of modified red mud, durability and corrosion resistance is an important aspect, which has been studied superficially and not in depth in this study.

(2) Because of the environmental pollution potential of red mud, the impact of red mud on the environment should also be monitored for a long period of time, but this study did not take into account this aspect of the research.

Data availability statement

The original contributions presented in the study are included in the article/Supplementary Material; further inquiries can be directed to the corresponding author.

Author contributions

ZD: methodology, validation, visualization, writing–original draft, and writing–review and editing. YC: conceptualization, data curation, resources, and writing–original draft. LJ: formal analysis, supervision, and writing–original draft. WW: software and writing–review and editing. SY: investigation and writing–review and editing.

Funding

The author(s) declare that financial support was received for the research, authorship, and/or publication of this article. This research was funded by the project on Green Low Carbon Design and High Resource Utilization of Concrete Materials (Funder: YC Funding number: SKDHKQ20240166) and the Research on Utilization Technology of Resourceful Highway Engineering of Stone Industry Waste Sludge (Sawdust) (Funder: YC Funding number: JS-22-1378).

Conflict of interest

The authors declare that the research was conducted in the absence of any commercial or financial relationships that could be construed as a potential conflict of interest.

Publisher's note

References

Da, L., Kaixi, J., Xunxiong, J., Feng, Z., Shengdong, W., Linyong, F., et al. (2022). Improving the A/S ratio of pretreated coal fly ash by a two-stage roasting for Bayer alumina production. *Fuel*, 310. (PC). doi:10.1016/J.FUEL.2021.122478

Department of Architectural Engineering, C. N. U., 99 Daehak-ro, Yuseong-gu, Daejeon 34134, Korea, Kang, S., and Kang, H. (2020). Mechanical properties of concrete containing liquefied red mud subjected to uniaxial compression loads. *Materials* 13 (4), 854. doi:10.3390/ma13040854

Dongshuai, H., Di, W., Xinpeng, W., Song, G., Rui, Y., Mengmeng, L., et al. (2021). Sustainable use of red mud in ultra-high performance concrete (UHPC): design and performance evaluation. *Cem. Concr. Compos.* 115, 103862. doi:10.1016/j.cemconcomp.2020.103862

Essaid, B., Hajar, B., Véronique, B., Hamid, M., Delia-Georgeta, D., Frédéric, B., et al. (2023). Phosphogypsum circular economy considerations: a critical review from more than 65 storage sites worldwide. *J. Clean. Prod.* 414, 137561. doi:10.1016/J.JCLEPRO.2023.137561

Falchetto, A., HoonMoon, K., Wang, D., and Riccardi, C. (2018). Investigation on the cooling medium effect in the characterization of asphalt binder with the bending beam rheometer (BBR). *Can. J. Civ. Eng.* 45 (7), 594–604. doi:10.1139/cjce-2017-0586

Gaole, H., wenwen, C., Zhen, Y., Ruiyang, Z., and Xiaoqiang, D. (2024). Study on the basic engineering properties of slag-silica ash solidifying red mud under alkali excitation. *J. Taiyuan Univ. Technol. Soc. Sci. Ed.*, 1–11. doi:10.16355/j.tyut.1007-9432.20230706

Hamidreza, A., Gholamreza, K., Abolhassan, N., Mesgari, A. S., and Masumeh, S. (2022). Metakaolin-red mud/carbon nanotubes geopolymer nanocomposite: mechanical properties and structural studies. *Mater. Res. Express* 9 (2), 025011. doi:10.1088/2053-1591/AC54D6

Hao, P. (2022). *Research on the road performance of roadbed filler based on modified red mud*. Guizhou, China: Guizhou University. doi:10.27047/d.cnki.ggudu.2022.002855

Hao, Y. (2023). *Experimental study on durability of red mud-based cementitious material stabilized base*. Shandong, China: Shandong University. doi:10.27272/d.cnki.gshdu.2023.001380

Hu, W., Ma, Y., Koehler, M., Gong, H., and Huang, B. (2021). Mix design optimization and early strength prediction of unary and binary geopolymer from multiple waste streams. *J. Hazard. Mater.* 403, 123632. doi:10.1016/j.jhazmat.2020.123632

Jiaolong, C., Na, Z., Heng, L., Xibin, Z., and Xiaoming, L. (2017). Hydration characteristics of red-mud based paste-like backfill material. *Chin. J. Eng.* 39 (11), 1640–1646. doi:10.13374/j.issn2095-9389.2017.11.005

Jingfu, Z., Hong, D., Mang, D., and Chang, S. (2007). Microstructure and properties of hydration products of slag-fly ash mixed cementitious materials. *J. Chin. Ceram. Soc.* (05), 633–637.

Juanhong, L., Zaibo, Z., Aixiang, W., and Yiming, W. (2020). Preparation and hydration mechanism of low concentration Bayer red mud filling materials. *Chin. J. Eng.* 42 (11), 1457–1464. doi:10.13374/j.issn2095-9389.2019.11.25.001

Khairul, M. A., Zanganeh, J., and Moghtaderi, B. (2019). The composition, recycling and utilisation of Bayer red mud. *Resour. Conserv. Recycl.* 141, 483–498. doi:10.1016/j.resconrec.2018.11.006

Lily, D. P., Emiliano, P., Marjan, T., David, H., Di, W., Peter, M., et al. (2022). RILEM interlaboratory study on the mechanical properties of asphalt mixtures modified with polyethylene waste. *J. Clean. Prod.* 375, 134124. doi:10.1016/J.JCLEPRO.2022.134124

Liu, R.-X., and Poon, C.-S. (2016a). Utilization of red mud derived from bauxite in self-compacting concrete. *J. Clean. Prod.* 112, 384–391. doi:10.1016/j.jclepro.2015.09.049

Liu, R.-x., and Poon, C.-S. (2016b). Effects of red mud on properties of self-compacting mortar. *J. Clean. Prod.* 135, 1170–1178. doi:10.1016/j.jclepro.2016.07.052

Luo, S., Liu, M., Yang, L., Chang, J., Yang, W., Yan, X., et al. (2019). Utilization of waste from alumina industry to produce sustainable cement-based materials. *Constr. Build. Mater.* 229, 116795. doi:10.1016/j.conbuildmat.2019.116795

Qiang, A., Huimin, P., Qingxin, Z., and Dongli, W. (2022). Strength development and microstructure of sustainable geopolymers made from alkali-activated ground granulated blast-furnace slag, calcium carbide residue, and red mud. *Constr. Build. Mater.* 356, 129279. doi:10.1016/J.CONBUILDMAT.2022.129279

Shan, J., Jiang, W., Huang, Y., Yuan, D., and Liu, Y. (2024). Unmanned aerial vehicle (UAV)-Based pavement image stitching without occlusion, crack semantic segmentation, and quantification. *IEEE Trans. Intell. Transp. Syst.*, 1–16. doi:10.1109/tits.2024.3424525

Shangjiefu, W., Huixin, J., Ershuai, L., Zhengxing, W., and Wei, G. (2023). Recovery of iron and aluminum from red mud, fly ash and phosphogypsum by co-sintering under alkaline control of carbon addition. *China Metall.* 33 (04), 119–126. doi:10.13228/j.boyuan.issn1006-9356.20220876

Sun, G., Ma, J., Sun, D., Li, B., Ling, S., and Luon, T. (2020a). Influence of thermal oxidative aging on temperature induced self-healing transition of polymer modified bitumens. *Mater. Des.* 192 (prepublish), 108717. doi:10.1016/j.matdes.2020.108717

Sun, G., Ma, J., Sun, D., and Yu, F. (2020b). Influence of weather accelerated ageing on healing temperature sensitivity of asphalts. *J. Clean. Prod.* 281, 124929. (prepublish). doi:10.1016/j.jclepro.2020.124929

Vigneshwaran, S., Uthayakumar, M., and Arumugaprabu, V. (2020). Potential use of industrial waste-red mud in developing hybrid composites: a waste management approach. *J. Clean. Prod.* 276 (prepublish), 124278. doi:10.1016/j.Jclepro.2020.124278

Walther, A., Büchler, S., Falchetto, A. C., Wang, D., Riccardi, C., and Wistuba, M. P. (2019a). Experimental investigation on asphalt mixtures prepared with reclaimed asphalt pavement and rejuvenators based on the BTSV method. *Road. Mater. Pavement Des.* 20 (7), 1695–1708. doi:10.1080/14680629.2019.1594053

Walther, A., Büchler, S., Falchetto, A. C., Wang, D., Riccardi, C., and Wistuba, M. P. (2019b). Experimental investigation on asphalt mixtures prepared with reclaimed asphalt pavement and rejuvenators based on the BTSV method. *Road. Mater. Pavement Des.* 20 (7), 1695–1708. doi:10.1080/14680629.2019.1594053

Wangjie, W., Chiara, C. M., Wei, J., and Nicole, K. (2024). Differing perspectives on the use of high-content SBS polymer-modified bitumen. *Constr. Build. Mater.* 411, 134433. doi:10.1016/J.CONBUILDMAT.2023.134433

Wei, J., Teng, W., Dongdong, Y., Aimin, S., Shuo, Z., Yufei, Z., et al. (2024). Available solar resources and photovoltaic system planning strategy for highway. *Renew. Sustain. Energy Rev.* 203, 114765. doi:10.1016/j.rser.2024.114765

Xi, L., Jintao, G., Xintuo, Q., and Zhancheng, G. (2022). An environmental-friendly method for recovery of soluble sodium and harmless utilization of red mud: solidification, separation, and mechanism. *Resour. Conserv. Recycl.* 186, 106543. doi:10.1016/J.RESCONREC.2022.106543

Xiangqun, D., Wei, X., and He, L. (2018). Effects of recycled concrete powder on the physical mechanical properties of wet-mixed mortar. *Concrete* 11, 94–97. doi:10.3969/j.issn.1002-3550.2018.11.024

Yang, Y., and Guozhong, L. (2008). Study on effect of silica fume and lithium salt on restraining alkali-aggregate reaction. *J. Build. Mater.* (04), 475–480. doi:10.3969/j.issn.1007-9629.2008.04.018

Yifan, G., Zhaofeng, L., Chen, Z., and Jian, Z. (2023). Study on occurrence form and solidification mechanism of alkaline components in red mud. *J. Mater. Cycles Waste Manag.* 25 (6), 3758–3775. doi:10.1007/S10163-023-01801-W

Yue, L., Yan, Z., Xuan, C., Weiwei, D., Rong, F., Luceille, O., et al. (2023). Micro-chemomechanical properties of red mud binder and its effect on concrete. *Compos. Part B* 258, 110688. doi:10.1016/j.compositesb.2023.110688

Yuxu, S., Zhaoyun, C., Haocheng, S., Xiangyu, L., Junqing, G., Chang, X., et al. (2024). Orthogonal optimization of the ratio of nano-silica sol-EVA-fly ash cement-based composite slurry and the effect on its physical properties. *J. China Coal Soc.*, 1–17. doi:10.13225/j.cnki.jccs.2023.0755

Zhang, N., Li, H., Zhao, Y., and Liu, X. (2016). Hydration characteristics and environmental friendly performance of a cementitious material composed of calcium silicate slag. *J. Hazard. Mater.* 306, 67–76. doi:10.1016/j.jhazmat.2015.11.055

Zhang, X., Zhu, F., Zhang, Y., Cai, J., Li, J., and Cao, Y. (2024). Comprehensive utilization of red mud and blast furnace dust: synergistic preparation of direct reduced iron and functional ceramsite. *Sep. Purif. Technol.* 345, 127436. doi:10.1016/J.SEPPUR.2024.127436

Zhongtao, L., Tianyi, Z., Lei, L., Jie, M., Meng, Z., Chongfei, T., et al. (2022). Solidification/stabilization of chromium slag in red mud-based geopolymer. *Constr. Build. Mater.* 316, 125813. doi:10.1016/j.conbuildmat.2021.125813